

Boosting the power conversion efficiency of perovskite solar cells based on Sn doped TiO₂ electron extraction layer via modification the TiO₂ phase junction

Ying-Han Liao^a, Yin-Hsuan Chang^a, Ting-Han Lin^a, Shun-Hsiang Chan^{a,b}, Kun-Mu Lee^{a,b,c}, Kai-Hsiang Hsu^c, Jen-Fu Hsu^{c,d,*}, Ming-Chung Wu^{a,b,c,*}

^a Department of Chemical and Materials Engineering, College of Engineering, Chang Gung University, Taoyuan 33302, Taiwan

^b Green Technology Research Center, Chang Gung University, Taoyuan 33302, Taiwan

^c Division of Neonatology, Department of Pediatrics, Chang Gung Memorial Hospital, Linkou, Taoyuan 33305, Taiwan

^d School of Medicine, College of Medicine, Chang Gung University, Taoyuan 33302, Taiwan

ARTICLE INFO

Keywords:

Perovskite solar cells
Sn-doped TiO₂
Phase junction
Electron extraction layer
Charge carrier mobility

ABSTRACT

Perovskite solar cells (PSCs) have earned considerable attention and are candidates against the inevitable energy crisis. Even though various successful PSCs have emerged, increasing the PCE by reinforcing charge collection is still a critical issue. The manipulation of carriers between the perovskite active layer and the electron extraction layer (EEL) is essential. Here, we prepared a tin-doped TiO₂ (Sn/TiO₂) EEL that presented two main polymorphs, anatase and rutile, and successfully fabricated a high-performance planar PSCs. Besides, the band alignment between EEL and perovskite active layer could be optimized by tuning the Sn doping concentration and the ratio of anatase and rutile phases. The intrinsic conductivity, interface morphology, band alignment, and charge carrier dynamic were characterized and the relationship to the photovoltaic performance was clarified. As the Sn ions being doped into TiO₂ structure, EEL presented the mixed TiO₂ rutile/anatase phase, directly narrowing the bandgap and promoting mobility. Furthermore, the adjustment of the band structure can facilitate electronic transitions. Finally, a promising planar PSC with Sn/TiO₂ phase junction EEL achieved a champion PCE of 15.4%.

1. Introduction

Among the new solar cell materials, perovskite has earned great attention attributable to their remarkable optical and electronic properties (Boyd et al., 2019; Cao et al., 2018; Domanski et al., 2018; Jeon et al., 2018; Liu, Z.F. et al., 2019). As ideal photovoltaic materials, perovskite shows long electron-hole diffusion length, high carrier mobility, and remarkable absorption coefficient (Luo et al., 2018; Ponseca et al., 2014; Stranks et al., 2013; Xing et al., 2013). Furthermore, its cost-effective and easy manufacturing process has made incredible progress in commercialization (Anaraki et al., 2016; Deng et al., 2015; Hwang et al., 2015; Li et al., 2018; Rong et al., 2018; Schmidt et al., 2015). Nowadays, many researchers devote themselves to improving the power conversion efficiency (PCE) and achieve an outstanding advance in PCE from 3.8% to 25.2% in only a few years (Burschka et al., 2013; <https://www.nrel.gov/pv/cell-efficiency.html>; Im et al., 2011; Kojima et al., 2009; Zhou et al., 2014). Even though various successful

PSCs have emerged, the charge collection is still an important issue. To increase the PCE, manipulating the carrier pathway between the perovskite active layer and the electron extraction layer (EEL) is essential. A smooth contact interface with the perovskite active layer plays a critical role in charge transport, photovoltaic performance, and charge recombination in PSCs. Hence, interfacial engineering is a necessary process for creating smooth and compact perovskite films which can reduce the carrier being trapped at the interface and recombination (Bai et al., 2018; Chen et al., 2018; Christians et al., 2018; Kumar et al., 2019; Liu et al., 2018; Son et al., 2018; Tress et al., 2018; Xu et al., 2016; Zeng et al., 2018).

The PCE enhancement can be achieved by introducing chlorine (Cl) into perovskite materials. The addition of Cl ions in halide perovskite material could effectively extend the electron diffusion length, increase surface coverage, and enhance the growth of perovskite grain boundaries (Cota-Leal et al., 2019; deQuillettes et al., 2015; Unger et al., 2014; Wang, K. et al., 2015; Yan et al., 2015; Yu et al., 2014; Zhu et al., 2015).

* Corresponding authors at: Chang Gung University, Taoyuan 33302, Taiwan.

E-mail addresses: hsujanfu@cgmh.org.tw (J.-F. Hsu), mingchungwu@cgu.edu.tw (M.-C. Wu).

<https://doi.org/10.1016/j.solener.2020.05.039>

Received 16 January 2020; Received in revised form 12 May 2020; Accepted 14 May 2020

0038-092X/ © 2020 International Solar Energy Society. Published by Elsevier Ltd. All rights reserved.

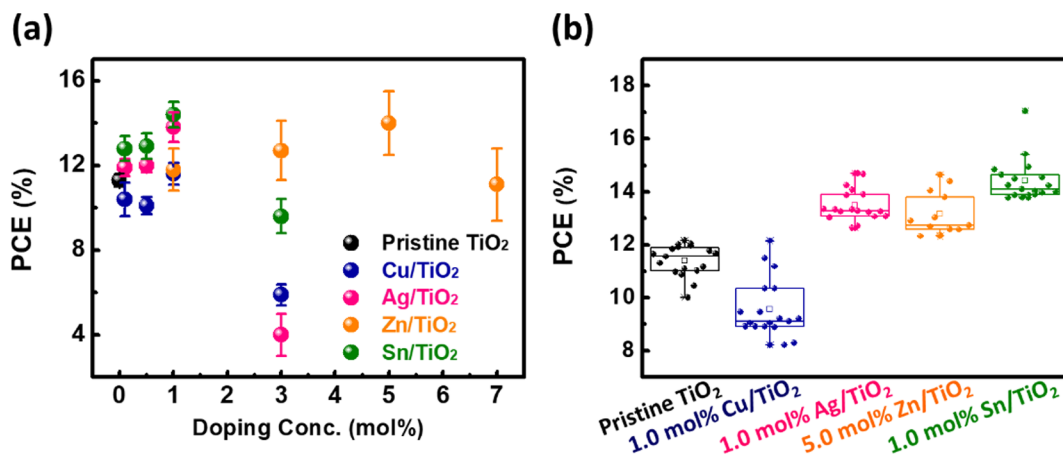


Fig. 1. (a) The average PCE of PSCs based on various metal-doped TiO₂ EEL with various doping levels, and (b) the PCE distribution of PSCs based on the optimized metal-doped TiO₂ EEL.

Table 1

RMS roughness and the calculated crystallite size of various Sn/TiO₂ layers, and RMS roughness of perovskite active layer deposited on various Sn/TiO₂ layer.

Sample	RMS roughness of TiO ₂ based EEL (nm)	RMS roughness of perovskite active layer (nm)	Crystallite size of TiO ₂ based EEL (nm)
Pristine TiO ₂	24.8	79.4	19.5
0.1 mol% Sn/TiO ₂	24.7	78.4	14.3
0.5 mol% Sn/TiO ₂	24.9	68.3	10.4
1.0 mol% Sn/TiO ₂	24.6	67.7	9.8
3.0 mol% Sn/TiO ₂	26.4	78.5	10.3

S. D. Stranks et al. studied the impact of electron diffusion length on PSCs based on CH₃NH₃PbI₃ and CH₃NH₃PbI_{3-x}Cl_x (deQuilettes et al., 2015; Nan et al., 2018). The CH₃NH₃PbI_{3-x}Cl_x devices exhibited a PCE of 12.2%, which was higher than the PCE of CH₃NH₃PbI₃ devices (~4.2%). Furthermore, introducing Cl ion could be advantageous to create a smooth interface between the EEL and perovskite active layer without the formation of a pinhole.

For EEL, TiO₂ is the most widely used material for PSCs, due to its low cost, non-toxicity, chemical durability, optical stability, suitable conduction band, and high charge mobility. According to previous research, the PSCs with only anatase phase junction EEL has only achieved a PCE of 9.8%. With only the rutile phase junction, the PSCs could improve to a PCE of 11.8% (Zhu et al., 2018). Hence, we considered that if PSCs can be based on TiO₂ with both anatase phase and rutile phase, it may simultaneously improve the V_{oc} and J_{sc}. The metal ion-doped TiO₂ as EEL has been studied thoroughly, and all of them showed superior electron junction and collection, conductivity, charge transport efficiency, and lower electron-hole recombination. As for dopant candidates, Nb (Kim et al., 2015; Liang et al., 2017), Mg (Wang, J. et al., 2015; Zhang et al., 2016), W (Xiao et al., 2017), Zn (Liu, X.T. et al., 2019; Wu, M.-C. et al., 2018a, Ag (Chen, S.H. et al., 2019; Lee and Chen, 2014; Wu, M.-C. et al., 2018b), and Sn (Cai et al., 2018; Qi et al., 2019; Su et al., 2016; Wang et al., 2019; Zhang et al., 2014) were proven to enhance the conductivity of TiO₂ EEL. Taking these advantages into consideration, we proposed an approach for metal-doped TiO₂ with a rutile/anatase mixed phase structure as EEL. Sn-doped TiO₂ has been applied in many fields such as visible-light photocatalysis, sodium-ion batteries, dye-sensitized solar cells, and PSCs. Sn ions mainly regulate the energy gap of TiO₂ which can be beneficial to the electron injecting into EEL from the active layer.

Here, we designed an EEL with Sn ions dopant into the rutile/anatase TiO₂ and successfully obtained a high-performance planar halide PSCs. Notably, the band alignment for EEL and halide perovskite active layer was controlled by Sn ions dopant in the mixed rutile/anatase TiO₂. In the study, a depth exploration of the structure and photovoltaic properties was carried out for Sn ions doped TiO₂. Further, Sn-doped

TiO₂ showed a more extensive range of absorption behavior and facilitated the electronic transitions. A promising planar PSC achieved a champion PCE at 15.4% and an average PCE of 14.4%.

2. Experimental details

All purchased chemicals were commercial sources and used for further preparation. The precursor solution of pristine TiO₂ and various Sn-doped TiO₂ (Sn/TiO₂) were obtained using the sol-gel method. A Ti sol-gel solution was independently prepared by slowly dropping 2.0 M HCl and titanium isopropoxide (Ti(OCH(CH₃)₂)₄, TTIP, > 97%, Sigma-Aldrich) in ethanol. Then, the acidic solution was added to TTIP precursor drop by drop under heavy stirring. For the Sn precursor solution, Tin(II) acetate (Sn(CH₃CO₂)₂) was successfully dissolved in a mixed solution of HCl and ethanol with various Sn molar ratio under vigorous stirring. The various Sn precursor solution was introduced into Ti precursor solution and stirred in an ice bath until they were well mixed. Thus, the pristine TiO₂ and Sn/TiO₂ precursor solutions were obtained.

The preparation of methylammonium iodide (CH₃NH₃I, MAI) followed a previous study (Wu, M.-C. et al., 2018a) by dissolving lead chloride (PbCl₂, 99.999%, Sigma-Aldrich) and MAI at a stoichiometric ratio of 39.0 wt% in 1.0 mL dimethylformamide (HCON(CH₃)₂, DMF, anhydrous, 99.8%, ACROS). After continuous stirring at 35 °C for 12 h, the CH₃NH₃PbI_{3-x}Cl_x perovskite precursor was obtained. The 2,2',7,7'-Tetrakis[*N,N*-di(4-methoxyphenyl)amino]-9,9'-spirobifluorene (spiro-OMeTAD, FrontMaterials Co. Ltd.) solution was prepared following our previous literature.

In the part of the PSCs device fabrication, the FTO glass (7 Ω, FrontMaterials Co. Ltd.) was first treated by UV-ozone to remove organic matters on the surface of FTO glass. The pristine TiO₂ and Sn/TiO₂ precursor solution were spin-coated on the FTO glasses followed by calcination at 550 °C to form the EEL. After that, the perovskite layer was prepared by spin-coated CH₃NH₃PbI_{3-x}Cl_x solution on TiO₂-based EELs at a rotational speed of 1200 rpm for 40 s. After, the spiro-OMeTAD solution was spin-coated onto CH₃NH₃PbI_{3-x}Cl_x layer at 2500 rpm for 30 s. Lastly, a 120 nm thick Ag electrode was deposited by

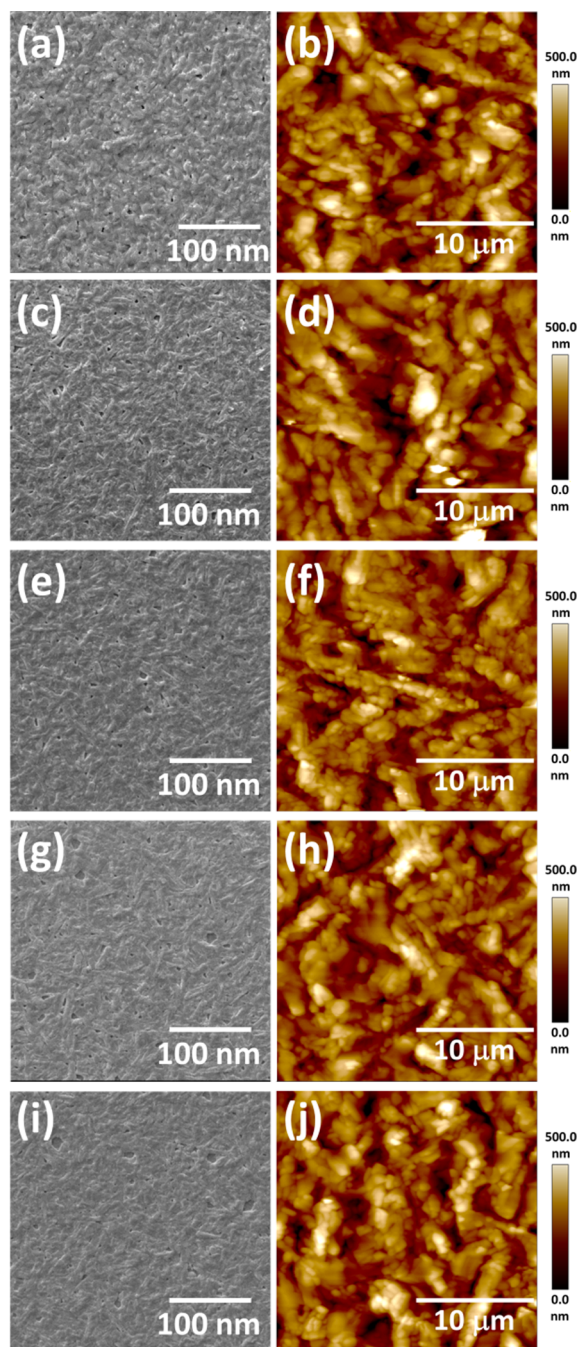


Fig. 2. Surface microstructure images and AFM topographic images of the perovskite films with various Sn/TiO₂ EEL, including (a, b) pristine TiO₂, (c, d) 0.1 mol% Sn/TiO₂, (e, f) 0.5 mol% Sn/TiO₂, (g, h) 1.0 mol% Sn/TiO₂, and (i, j) 3.0 mol% Sn/TiO₂.

thermal evaporation method with a shadow mask, making a 0.09 cm² active area.

The crystal structure of Sn/TiO₂ EEL was characterized by the X-ray diffractometer (XRD, Bruker, D2 phaser with Xflash 430, Germany). The surface morphology and topography of Sn/TiO₂ EEL with various Sn dopant concentration and perovskite films based on various Sn/TiO₂ EEL were observed by field-emission scanning electron microscope (FE-SEM, SU8010, Hitachi), SEM (SNE-4500 M, SEC), and atomic force microscope (AFM) (Bruker Multimode2-U-NSV, Bruker). To investigate the absorption properties of various TiO₂ EEL, UV-Vis spectrometer (V-730, Jasco) was used. The photoluminescence (PL) spectra were detected by using a 440 nm continuous-wave diode laser (PDLH-440-25,

DongWoo Optron Co.Ltd). The time-resolved photoluminescence (TRPL) spectra of the perovskite active layer coated on Sn/TiO₂ EEL were observed using time-correlated single-photon counting (TCSPC) taken under 440 nm pulse laser (WELLS-001 FX, DongWoo Optron Co. Ltd.). For the I–V characteristics, computer-controlled digital source meter (Keithley 2410, Keithley, OH, USA) was used under 1.0 sun illumination (100 mW/cm², AM 1.5G). The simulated AM 1.5 sunlight was generated using irradiation (Newport-69920, 100 mW/cm²) calibrated with a silicon reference cell (Oriel P/N 91150V, VLSI standards) with KG-5 visible color filter. X-ray photoelectron spectrometer (K-Alpha X-ray photoelectron spectrometer, Thermo Fisher Scientific) was used to investigate the chemical composition of Sn/TiO₂ EEL. The energy levels of the pristine TiO₂ layer and 1.0 mol% Sn/TiO₂ layer were obtained by ultraviolet photoelectron spectroscopy (UPS) (PHI 5000 VersaProbe, ULVAC-PHI) using an ultraviolet light source of He I emission (21.2 eV, B50 W) and take-off angle of 90°.

3. Results and discussion

Doping suitable metal ion into the TiO₂ lattice could tune the bandgap and trap states efficiently. Lots of studies have demonstrated that metal doping can modify the TiO₂ conduction band minimum (CBM) and valence band maximum (VBM) level, which further improve the photovoltaic properties of TiO₂, increasing the short-circuit current density (J_{sc}) or the open-circuit voltage (V_{oc}) of PSCs. In previous works, we have tried to dope Cu, Ag, and Zn into TiO₂ and the PCE of PSC based on various metal-doped TiO₂ EEL are shown in Fig. 1a (Cao et al., 2018; Chen, S.H. et al., 2019; Wu et al., 2016a; Wu, M.-C. et al., 2018b; Wu et al., 2018c). The PCE distribution of devices with optimized metal-doped is shown in Fig. 1b. TiO₂ EEL Cu/TiO₂ is known for its narrow bandgap energies and high light-absorption coefficients. At the optimum Cu concentration of 1.0 mol%, the average PCE can achieve 11.6%. Doping Ag into TiO₂ lattice significantly enlarges the J_{sc} because of its high electrical conductivity. The optimal Ag/TiO₂ doping concentration is 1.0 mol% with the average PCE achieving 13.8%. The low-cost Zn is also a candidate for metal doping due to its high electrical conductivity. The optimal Zn/TiO₂ doping concentration is 5.0 mol% with the average PCE achieving 14.0%. In the present study, we further doped Sn into TiO₂ lattice and found that the PCE is even higher than Cu/TiO₂, Ag/TiO₂, and Zn/TiO₂. The optimal Sn/TiO₂ doping concentration is 1.0 mol% with the average PCE achieving 14.4%. Therefore, we thoroughly investigated the Sn/TiO₂ in this work.

The interface between the perovskite active layer and Sn/TiO₂ EEL is a crucial factor in the charge transport properties. To analyze the influence of the interface on the electron transport effect, we used the multi-functional FE-SEM and AFM to observe the surface morphology of various Sn/TiO₂ layers (Fig. S1). Looking at the demonstration of morphology and topographic images, we discovered that the TiO₂ with the Sn doping, it would not affect RMS roughness dramatically (Table 1). Therefore, as we further deposit perovskite active layer onto the as-prepared (Sn/TiO₂)/FTO. The SEM and AFM images of perovskite active layer are shown in Fig. 2. The RMS first decreased, which indicated that the surface morphology became smoother due to the less roughness of 1.0 mol% Sn/TiO₂ layer, it could be more suitable for fabricating high-efficiency PSCs. Until the doping level up to 3.0 mol%, the RMS increases which has a minor impact on the perovskite active layer. The RMS roughness of the perovskite active layer deposited on various Sn/TiO₂ EEL is summarized in Table 1.

The series of TiO₂ with various Sn doping levels were calcined at 550 °C in the air for 12 h. The crystal structures of Sn/TiO₂ were obtained by XRD (Fig. 3a). Pristine TiO₂ calcined at 550 °C in the air for 12 h possesses the single anatase crystal phase. The diffraction peaks of pristine TiO₂ at 2θ around 25.3°, 37.8°, and 48.2° can be ascribed to the tetragonal structure with unit cell parameters $a = 3.78 \text{ \AA}$ and $c = 9.51 \text{ \AA}$ [JCPDS 21-1272]. As we increased the amount of Sn dopant, it was transformed into a higher proportion of rutile crystal phase.

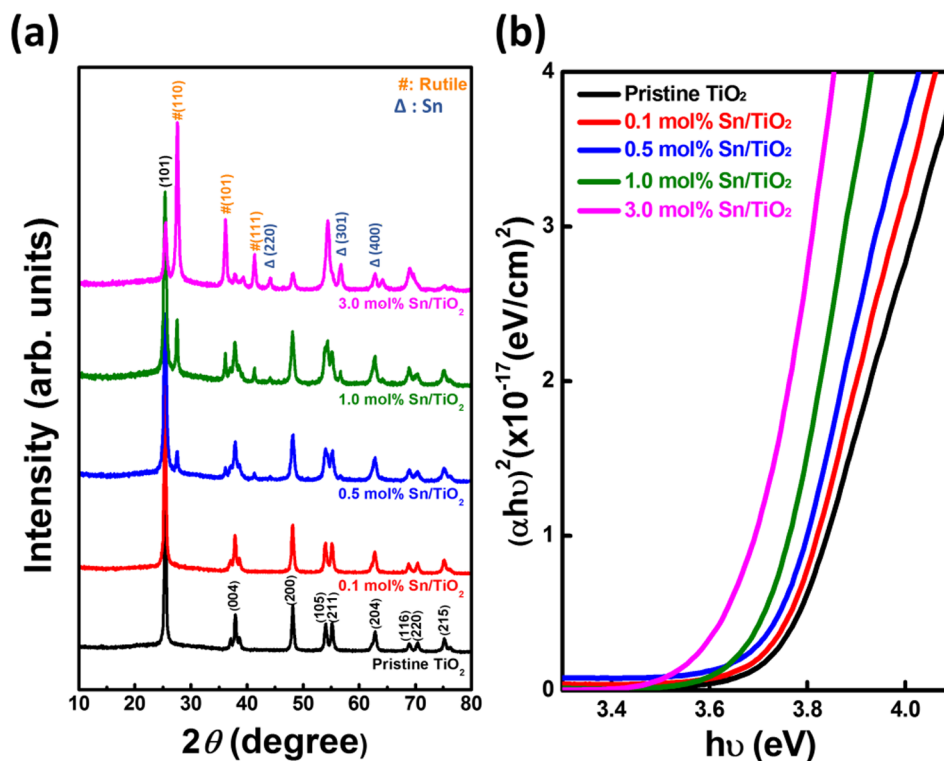


Fig. 3. (a) XRD patterns and (b) Tauc plots of Sn/TiO₂ EEL with various Sn doping levels calcined at 550 °C in the air for 12 h.

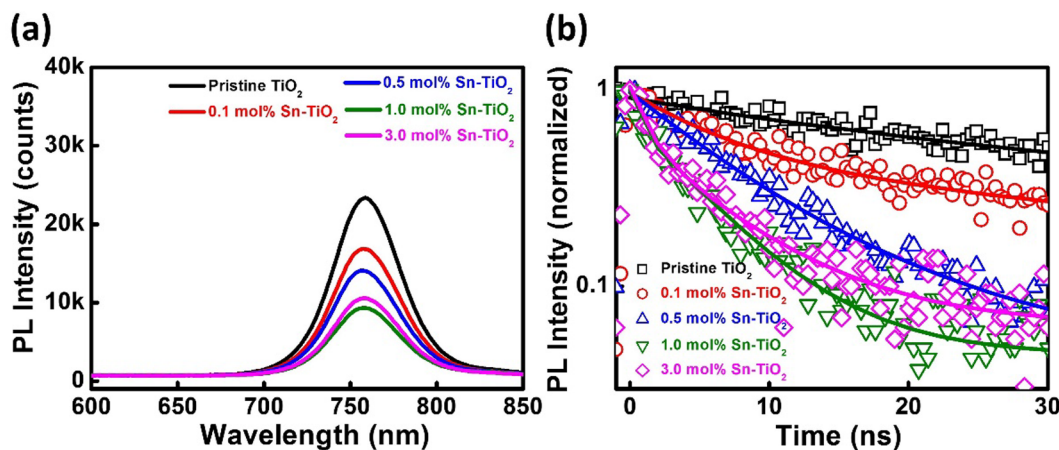


Fig. 4. (a) PL spectra and (b) transient TRPL plots of the device based on the following structure: CH₃NH₃PbI_{3-x}Cl_x/(Sn/TiO₂)/FTO.

Table 2

Summary of fast decay time (τ_1), slow decay time (τ_2), and PL average decay time (τ_{avg}) for CH₃NH₃PbI_{3-x}Cl_x/(Sn/TiO₂)/FTO.

Sample name	A (%)	τ_1 (ns)	B (%)	τ_2 (ns)	τ_{avg} (ns)
Pristine TiO ₂	21.6	14.4	62.8	62.7	47.5
0.1 mol% Sn/TiO ₂	51.9	6.1	37.3	45.4	23.5
0.5 mol% Sn/TiO ₂	73.7	6.6	20.3	17.5	9.7
1.0 mol% Sn/TiO ₂	66.8	0.2	28.9	5.4	3.8
3.0 mol% Sn/ TiO ₂	46.6	1.2	50.7	6.8	4.1

Based on our previous work (Wu et al., 2016a; Wu et al., 2016b; Wu et al., 2017; Wu, M.-C. et al., 2018a), to obtain the phase transformation through the calcination process, the calcination temperature must be higher than 700 °C (Wu et al., 2015). As the Sn doping level reached 0.50 mol%, the characteristic peak of rutile phase started appearing (2θ ~ 27.5°, 36.1°, and 41.3°). Meanwhile, the characteristic peak of

anatase decreased. We also used Scherrer equation (Eq. (1)) to calculate the average crystallite size corresponding to (1 0 1) plane as shown in Table 1.

$$D = \frac{K\lambda}{\beta \cos\theta} \quad (1)$$

where D is the mean size of the ordered crystalline, K , the shape factor, is ~0.9, λ is the incident X-ray wavelength given for CuK α -radiation (~1.54 Å), β is FWHM in radians, and θ is Bragg angle in degree. With increasing Sn doping levels, the crystallite size of the anatase TiO₂ gradually decreased due to the formation of rutile phase. It is interesting to know that Sn doped into TiO₂ can facilitate the formation of rutile TiO₂. Therefore, Sn doping can promote the transformation of TiO₂ from anatase phase to rutile phase. These results are notably unique compared to other TiO₂ nanomaterial doped with metals such as Zn, Ag, Bi, Nb, and Cu in previous studies (Chan et al., 2017; Chang and Wu, 2019; Wu, M.-C. et al., 2018b; Wu et al., 2018d). Besides, increase

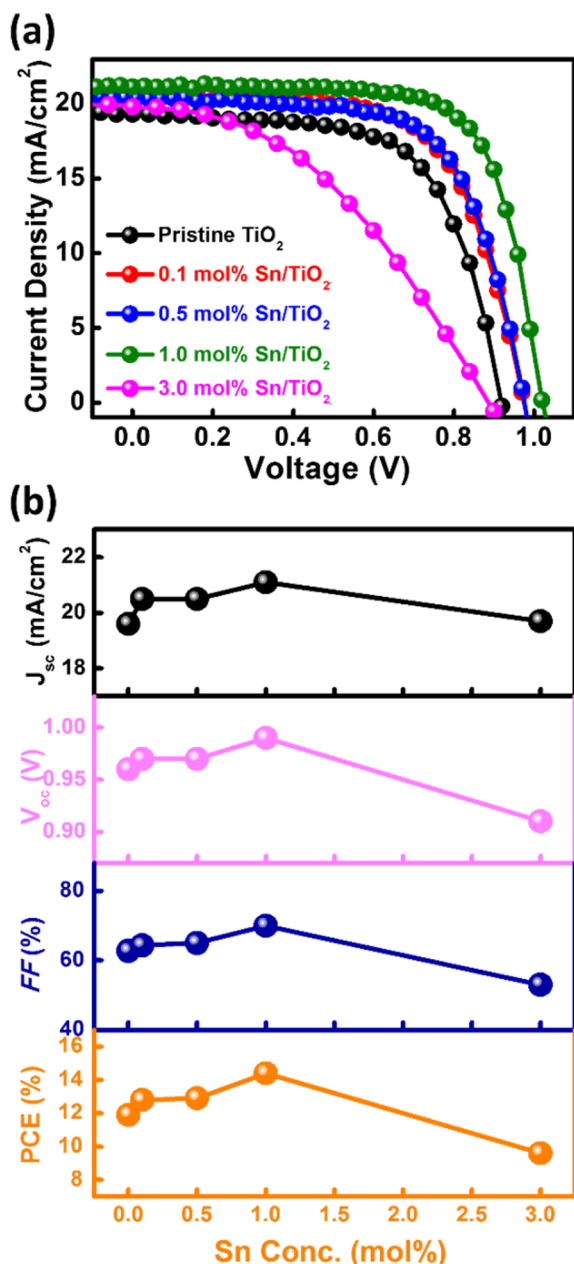


Fig. 5. (a) J-V characteristics of PSCs based on various Sn/TiO₂ EEL, and (b) the correlation between photovoltaic characteristics (V_{oc} , J_{sc} , FF and PCE) and Sn doping concentration.

Table 3

The detailed photovoltaic parameters of PSCs based on various TiO₂ EEL.

Sample Name	V_{oc} (V)	J_{sc} (mA/cm ²)	FF (%)	PCE (%)
Pristine TiO ₂	0.93 ± 0.03	19.4 ± 0.2	63.0 ± 1.8	11.3 ± 0.3
0.1 mol% Sn/TiO ₂	0.97 ± 0.03	20.6 ± 0.5	64.3 ± 2.4	12.9 ± 0.6
0.5 mol% Sn/TiO ₂	0.97 ± 0.03	20.5 ± 0.6	65.0 ± 2.0	12.9 ± 0.6
1.0 mol% Sn/TiO ₂	0.99 ± 0.02	21.0 ± 0.9	69.4 ± 3.7	14.4 ± 0.8
3.0 mol% Sn/TiO ₂	0.89 ± 0.02	19.1 ± 1.3	44.0 ± 4.4	7.5 ± 1.2

the concentration of Sn in TiO₂ to 3.0 mol% may lead to precipitation of Sn, which can be verified by XRD patterns in Fig. 3a. Tauc plots converted by UV/Vis absorption spectra were seen remarkably red-shifted, as shown in Fig. 3b. The measured bandgap for pristine TiO₂ is 3.72 eV. The bandgap of 3.0 mol% Sn/TiO₂ is about 3.67 eV. The reduced bandgap is ascribed to the conduction band shifting. Another possible

reason is that the energy gap of the rutile phase of titanium dioxide is lower than that of the anatase phase. We speculated that the edge shift of the conduction band is beneficial to the migration of the electron from the perovskite active layer to Sn/TiO₂ EEL. Besides, the elemental compositions of various Sn/TiO₂ EELs were investigated by XPS (Fig. S2). From these spectra, it could be seen clearly that, while increasing the amount of Sn dopant, the Sn 3d signal was enhanced obviously (Fig. S2d). Nevertheless, compared to the binding energy of pristine TiO₂, the binding energy position for Ti shows no shift after doping Sn into TiO₂ (Fig. S2a). The XPS spectra confirm that doping Sn does not destroy the crystal structure of TiO₂.

PL spectra and TRPL decay characterization for CH₃NH₃PbI_{3-x}Cl_x/ (Sn/TiO₂)/FTO were conducted to confirm the charge carrier dynamics. Fig. 4a is the PL spectra excited by 440 nm light. The CH₃NH₃PbI_{3-x}Cl_x coated on pristine TiO₂ demonstrated the strongest PL quenching efficiency among various Sn/TiO₂ layers suggesting that Sn dopant can promote the carrier extraction performance at the interface between perovskite active layer and Sn/TiO₂ EEL. The 1.0 mol% Sn/TiO₂ with the densest morphology makes the perovskite active layer coating process much easier to form a smooth interface and shows a high coverage. Therefore, the less defect on the interface of CH₃NH₃PbI_{3-x}Cl_x/1.0 mol% Sn/TiO₂, the less the carriers be trapped at the defect and thus CH₃NH₃PbI_{3-x}Cl_x/1.0 mol% Sn/TiO₂ exhibits the lowest PL quenching efficiency. The transient PL decay behavior was also investigated as shown in Fig. 4b. The results verified the carrier transfer and separation behavior. The exponential decay kinetics function (Eq. (2)) was adopted to fit the transient PL decay plots.

$$F(t) = A \exp\left(-\frac{t}{\tau_1}\right) + B \exp\left(-\frac{t}{\tau_2}\right) \quad (2)$$

where τ_1 and τ_2 are fast and slow decay time, respectively. A and B are the time-independent coefficient of amplitude fraction. All of the fitting data are listed in Table 2. The average PL lifetime (τ_{avg}) is estimated using the following equation:

$$\tau_{avg} = \frac{A\tau_1 + B\tau_2}{(A + B)} \quad (3)$$

Compare to the pristine TiO₂, all CH₃NH₃PbI_{3-x}Cl_x coated Sn/TiO₂ showed rapid PL decay. The device with pristine TiO₂ showed a fast decay time of 14.4 ns. Notably, the fast decay time of the device based on 1.0 mol% Sn/TiO₂ is decreased to 0.2 ns. The CH₃NH₃PbI_{3-x}Cl_x/1.0 mol% Sn/TiO₂ showed the shortest PL average lifetime (3.8 ns) which indicated that the charge injected quickly from perovskite active layer into 1.0 mol% Sn/TiO₂ EEL. The high electron injection rate could be beneficial for increasing the overall performance of PSCs. The efficient carrier injection could hinder the radiative electron-hole recombination at the interface of perovskite active layer/EEL. Besides, the other factor could be the anatase/rutile mixed-phase TiO₂ helping the electron transport from perovskite active layer to EEL.

The structure of as-prepared PSCs device is FTO substrate/(Sn/TiO₂)/CH₃NH₃PbI_{3-x}Cl_x/Spiro-OMeTAD/Ag. The photocurrent density-voltage (J-V) of PSCs based on Sn/TiO₂ EEL with various Sn doping levels are shown in Fig. 5a. The summarized photovoltaic performances of various Sn/TiO₂ PSCs were reported in Fig. 5b and Table 3. For the device with 1.0 mol% Sn/TiO₂ EEL, the J_{sc} increased from 19.4 to 21.0 mA/cm² and V_{oc} increased from 0.93 to 0.99 V. We proposed that the enhanced photovoltaic performance could be due to the mixed-phase Sn/TiO₂ obtaining the higher charge carrier mobility compared to that of the pristine TiO₂. When Sn doping level further increased to 3.0 mol%, the fill factor (FF) was dramatically decreased, and the average PCE decreased to 7.5%. The result indicated that the decline in photovoltaic performance might be caused by the unexpected electron trap at the rough interface of perovskite active layer/3.0 mol% Sn/TiO₂ EEL, and thus, hindering the carrier transmission.

We further calcined the pristine TiO₂ and 1.0 mol% Sn/TiO₂ at

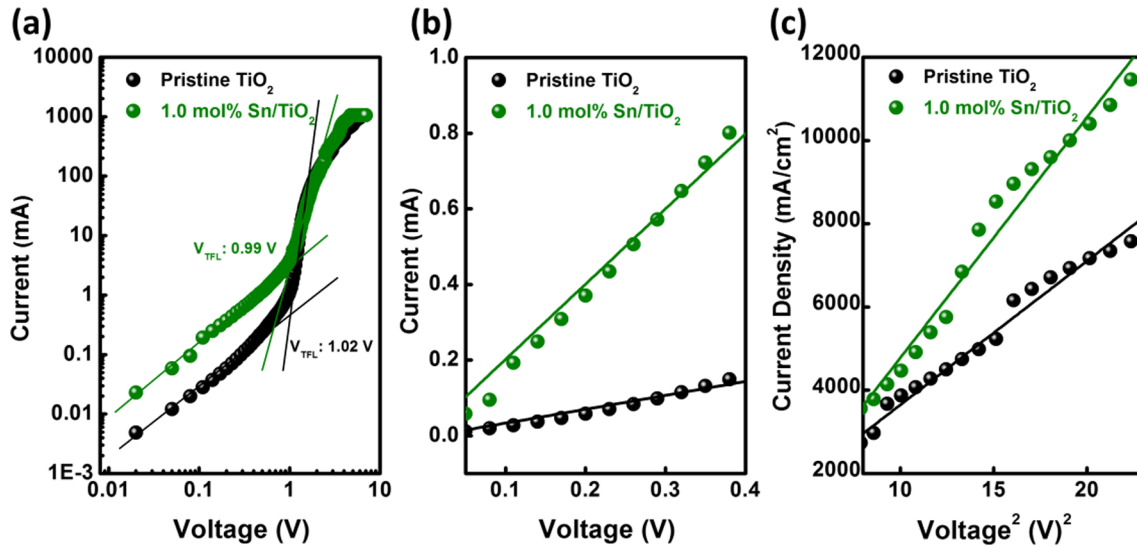


Fig. 6. (a) J-V curves of the device with the following structure: Au/TiO₂/FTO glass with pristine TiO₂ and 1.0 mol% Sn/TiO₂. (b) I-V curves of ohmic region ($I \propto V$) and (c) J-V² curve of Child's region ($I \propto V^2$).

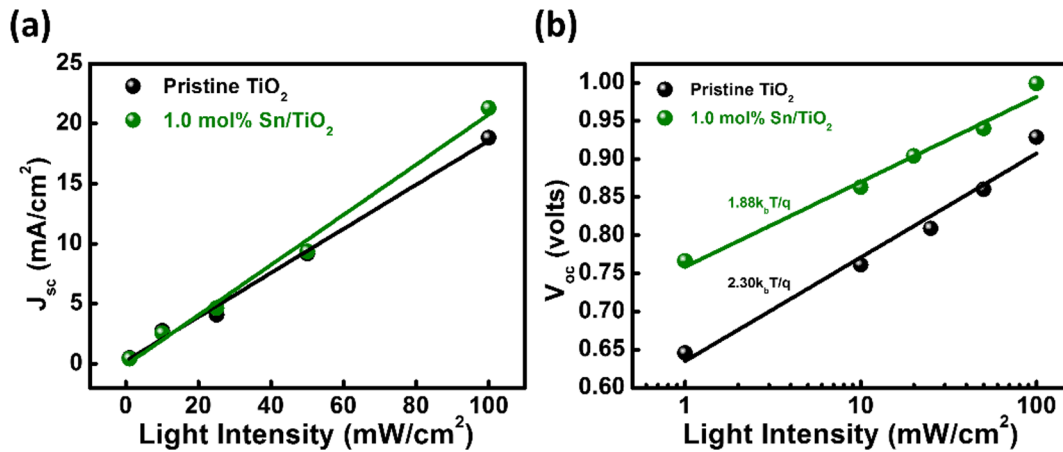


Fig. 7. Light intensity dependence of PSCs based on pristine TiO₂ and 1.0 mol% Sn/TiO₂ EEL. (a) J_{sc} versus light intensity and (b) V_{oc} versus light intensity.

various O₂/N₂ atmospheres and studied the changes after the calcination process. By alternating the amount of oxygen fed during the calcination process, we can tune the formation of Ti³⁺ and oxygen vacancy efficiently. For the existence of Ti³⁺ and oxygen vacancy, these defects formed trap states in the bandgap, and therefore impeded the photoelectrons injection into the EEL from the perovskite active layer. We measured the J-V curves and the detailed photovoltaic characteristics of PSCs based on pristine TiO₂ EEL and 1.0 mol% Sn/TiO₂ EEL calcined under various O₂/N₂ atmospheres (Fig. S3 and Table S1). Oxygen vacancies located at the surface TiO₂ could be the traps for photoexcited electrons. The decreasing of oxygen vacancies could facilitate the injection of photoexcited electron from perovskite to TiO₂. Therefore, while calcined in the atmospheres with the presence of oxygen, the V_{oc} and J_{sc} increased compare to those of EEL calcined under N₂ atmosphere. The optimal calcination condition is in 20% O₂ in N₂ for both pristine TiO₂ and 1.0 mol% Sn/TiO₂. The champion PSCs based on 1.0 mol% Sn/TiO₂ calcined in 20% O₂ in N₂ reached a PCE as high as 15.4%.

The space-charge-limited current (SCLC) measurement in Au/TiO₂/FTO glass with pristine TiO₂ and 1.0 mol% Sn/TiO₂ was performed to evaluate the electron trap density in TiO₂ films (Fig. 6a). The dense Au film was slowly deposited on the TiO₂/FTO glass with a thickness of ~ 120 nm at a rate of 0.1 Å s⁻¹. The SCLC measurement is often followed by three regimes: (i) ohmic region ($I \propto V$) to calculate the

electrical conductivity, (ii) TFL region ($I \propto V^n$, $n > 2$) to estimate the trap density, and (iii) Child's region ($I \propto V^2$) to determine the charge mobility. In the ohmic region as shown in Fig. 6b, the I-V curves reveal linear behavior and follow the equation as below,

$$I = \sigma_0(A/d)V \quad (4)$$

where A , d , and σ_0 are sample area, thickness, and electrical conductivity, respectively. The electrical conductivity promoted from 3.29×10^{-7} mS/cm to 1.78×10^{-6} mS/cm as the doping level increased to 1.0 mol%. The trap filled limit voltage (V_{TFL}), located at the transition point between the ohmic and TFL region, is associated with trap density (N_t) as the equation below.

$$V_{TFL} = \frac{eN_t d^2}{2\epsilon\epsilon_0} \quad (5)$$

where e is an elementary charge, ϵ is the dielectric constant of TiO₂, and ϵ_0 is the permittivity of free space. The N_t of pristine TiO₂ and 1.0 mol% Sn/TiO₂ are calculated to be 1.00×10^{13} cm⁻³ and 9.73×10^{12} cm⁻³, respectively. As the bias voltage was increased to 3.0 V, the current would be determined by charge carriers injected from the contacts. Then, the current only depends on the mobility rather than the charge carrier density. Therefore, the charge carrier mobility (μ) can be calculated by Mott-Gurney law in the Child's region (Fig. 6c):

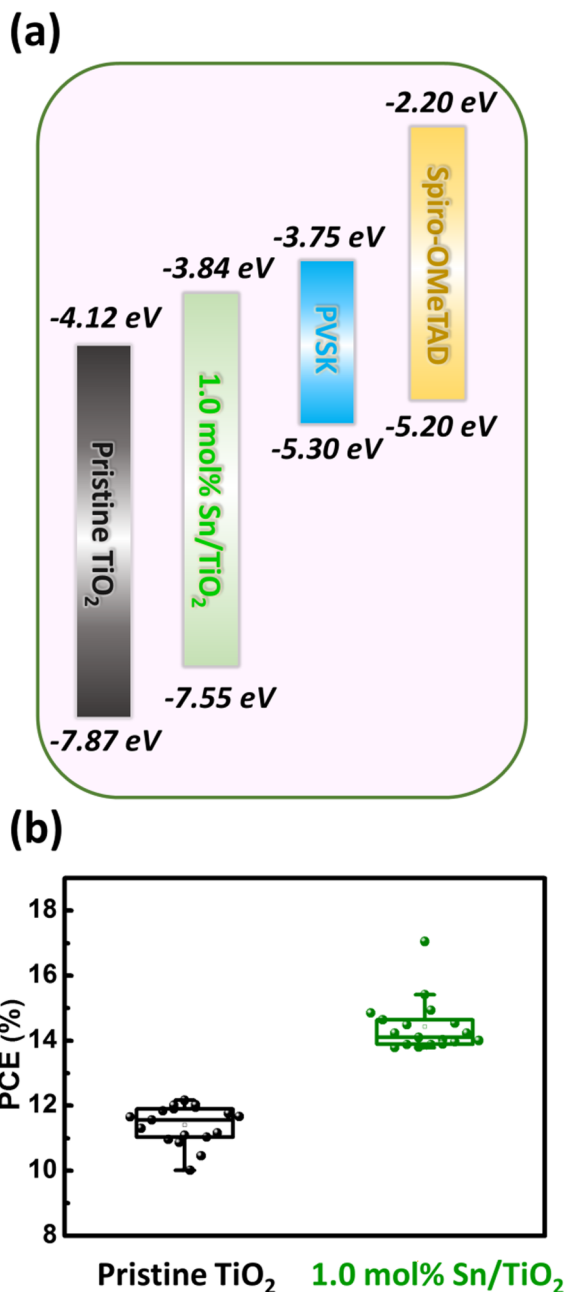


Fig. 8. (a) Scheme of energy level diagram for pristine TiO₂, 1.0 mol% Sn/TiO₂, perovskite active layer and hole transport layer (Da et al., 2018) and (b) PCE distribution of the PSCs based on pristine TiO₂ and 1.0 mol% Sn/TiO₂.

$$J = \frac{9}{8} \mu \epsilon \epsilon_0 \frac{V^2}{d^3} \quad (6)$$

where ϵ_0 and ϵ represent the permittivity of free space and dielectric constant of TiO₂. The μ of pristine TiO₂ and 1.0 mol% Sn/TiO₂ were $3.16 \times 10^{-7} \text{ cm}^2 \text{ V}^{-1} \text{ s}^{-1}$ and $5.28 \times 10^{-7} \text{ cm}^2 \text{ V}^{-1} \text{ s}^{-1}$, respectively. According to the results, 1.0 mol% Sn/TiO₂ presented the higher charge carrier mobility which facilitates the carrier migration more efficiently while the PSC is excited by the light. Thus, the photovoltaic performance for the PSCs based on 1.0 mol% Sn/TiO₂ could be successfully improved.

The charge recombination mechanism of PSCs based on pristine TiO₂ and 1.0 mol% Sn/TiO₂ was clarified by measuring light intensity-dependent J-V characteristics. The relationship between J_{sc} depends linearly on light intensity (Fig. 7a). The increase of V_{oc} with respect to light intensity is followed by the function as shown below

$$V_{oc} = V_s + \frac{nk_B T}{q} \ln \frac{P}{P_s} \quad (7)$$

where V_s is the open-voltage at 100 mW cm^{-2} , n is an ideal factor, k_B is the Boltzmann constant, T is the absolute temperature (298.15 K), q is the elementary charge, P is the light intensities, and P_s is standard light intensity (100 mW cm^{-2}). Fig. 7b shows the semi-log plots of V_{oc} versus light intensity. The n value are 2.30 and 1.88 $\frac{k_B T}{q}$, for PSCs based on pristine TiO₂ and 1.0 mol% Sn/TiO₂, respectively. In general, when n approaches 2, it indicates that the PSCs is dominated by trap-assisted recombination. Based on this result, we could suggest that doping Sn into TiO₂ is beneficial to reduce the trap-assisted recombination.

As mentioned, doping Sn into TiO₂ can decrease bandgap and modify the energy level of the valence band (VB) and conduction band (CB). The shift of the VB and CB could be revealed by UPS (Fig. S4). The energy level diagram (Fig. 8a) of pristine TiO₂ and 1.0 mol% Sn/TiO₂ were produced by converting and combining the results of UPS and UV-Vis spectra. The VB maximum and CB minimum for pristine TiO₂ were -7.87 and -4.12 eV, respectively. The VB maximum and CB minimum for 1.0 mol% Sn/TiO₂ were -7.55 and -3.84 eV, respectively. As a result, doping Sn could tune the position of VB and CB effectively. Due to the appropriate band alignment, the charge transport efficiency can be improved by the enhanced band structure of TiO₂. The PCE distribution was obtained by measuring 18 devices of each the pristine TiO₂ EEL and the 1.0 mol% Sn/TiO₂ EEL to confirm that 1.0 mol% Sn/TiO₂ EEL shows high performance. The average PCE of PSCs with 1.0 mol% Sn/TiO₂ EEL was higher than that of PSCs with pristine TiO₂ EEL.

4. Conclusion

In summary, we successfully fabricated Sn/TiO₂ and used it as the EEL for high-performance PSCs. When doping Sn into TiO₂, it facilitates the formation of anatase/rutile phase junction at a fixed calcination temperature of 550 °C. Compare to pristine TiO₂ with pure anatase phase, the mixed-phase TiO₂ successfully decreased bandgap and showed the higher charge carrier mobility. Thus, the photovoltaic performance for the PSCs with 1.0 mol% Sn/TiO₂ can be improved. When Sn doping level was set to 1.0 mol%, the average V_{oc} increased to 0.99 from 0.93 V and the average J_{sc} increased to 21.0 from 19.4 mA/cm². Finally, the PCE of PSCs with 1.0 mol% Sn/TiO₂ can be enhanced to 14.4%, and the champion device of PSCs reached a PCE as high as 15.4%.

Declaration of Competing Interest

The authors declare that they have no known competing financial interests or personal relationships that could have appeared to influence the work reported in this paper.

Acknowledgments

The authors appreciate Prof. Wei-Fang Su at National Taiwan University and Dr. Ming-Tao Lee (BL-13A1) and Dr. Jyh-Fu Lee (BL-17C1) at National Synchrotron Radiation Research Centre for useful discussion and suggestions. The financial support from Ministry of Science and Technology, Taiwan (Project No. 106-2221-E-182-057-MY3, 108-2119-M-002-005, and 108-3116-F-002-002-CC2), Chang Gung University (QZRPD181) and Chang Gung Memorial Hospital, Linkou (CMRPD2H0162 and BMRPC74) are highly appreciated.

Appendix A. Supplementary material

Supplementary data to this article can be found online at <https://doi.org/10.1016/j.solener.2020.05.039>.

References

- Anaraki, E.H., Kermanpur, A., Steier, L., Domanski, K., Matsui, T., Tress, W., Saliba, M., Abate, A., Grätzel, M., Hagfeldt, A., Correa-Baena, J.P., 2016. Highly efficient and stable planar perovskite solar cells by solution-processed tin oxide. *Energy Environ. Sci.* 9, 3128–3134.
- Bai, Y., Meng, X.Y., Yang, S.H., 2018. Interface engineering for highly efficient and stable planar p-i-n perovskite solar cells. *Adv. Energy Mater.* 8, 1701883.
- Boyd, C.C., Cheacharoen, R., Leijtens, T., McGehee, M.D., 2019. Understanding degradation mechanisms and improving stability of perovskite photovoltaics. *Chem. Rev.* 119, 3418–3451.
- Burschka, J., Pellet, N., Moon, S.-J., Humphry-Baker, R., Gao, P., Nazeeruddin, M.K., Grätzel, M., 2013. Sequential deposition as a route to high-performance perovskite sensitized solar cells. *Nature* 499, 316.
- Cai, Q.B., Zhang, Y.Q., Liang, C., Li, P.W., Gu, H., Liu, X.T., Wang, J.F., Shentu, Z.X., Fan, J.J., Shao, G.S., 2018. Enhancing efficiency of planar structure perovskite solar cells using Sn-doped TiO₂ as electron transport layer at low temperature. *Electrochim. Acta* 261, 227–235.
- Cao, J., Wu, B.H., Chen, R.H., Wu, Y.Y.Q., Hui, Y., Mao, B.W., Zheng, N.F., 2018. Efficient, hysteresis-free, and stable perovskite solar cells with ZnO as electron-transport layer: effect of surface passivation. *Adv. Mater.* 30, 1705596.
- Chan, S.-H., Wu, M.-C., Lee, K.-M., Chen, W.-C., Lin, T.-H., Su, W.-F., 2017. Enhancing perovskite solar cell performance and stability by doping barium in methylammonium lead halide. *J. Mater. Chem. A* 5, 18044–18052.
- Chang, Y.-H., Wu, M.-C., 2019. Enhanced photocatalytic reduction of Cr(VI) by combined magnetic TiO₂-based NFs and ammonium oxalate hole scavengers. *Catalysts* 9, 1–2.
- Chen, G.-S., Chen, Y.-C., Lee, C.-T., Lee, H.-Y., 2018. Performance improvement of perovskite solar cells using electron and hole transport layers. *Sol. Energy* 174, 897–900.
- Chen, S.-H., Chan, S.-H., Lin, Y.-T., Wu, M.-C., 2019. Enhanced power conversion efficiency of perovskite solar cells based on mesoscopic Ag-doped TiO₂ electron transport layer. *Appl. Surf. Sci.* 469, 18–26.
- Christians, J.A., Schulz, P., Tinkham, J.S., Schloemer, T.H., Harvey, S.P., de Villiers, B.J.T., Sellinger, A., Berry, J.J., Luther, J.M., 2018. Tailored interfaces of unencapsulated perovskite solar cells for > 1,000 hour operational stability. *Nat. Energy* 3, 68–74.
- Cota-Leal, M., García-Valenzuela, J.A., Cabrera-German, D., Martínez-Gil, M., Paredes-Sotelo, E., Sotelo-Lerma, M., 2019. Synthesis of CH₃NH₃PbI_{3-x}Cl_x perovskite by the three-step route consisting of chemical solution deposition followed by gas-solid reaction transformations: Film quality and photodetector performance evaluation. *Org. Electron.* 73, 76–86.
- Da, Y., Xuan, Y., Li, Q., 2018. Quantifying energy losses in planar perovskite solar cells. *Sol. Energy Mater. Sol. Cells* 174, 206–213.
- Deng, Y.H., Peng, E., Shao, Y.C., Xiao, Z.G., Dong, Q.F., Huang, J.S., 2015. Scalable fabrication of efficient organolead trihalide perovskite solar cells with doctor-bladed active layers. *Energy Environ. Sci.* 8, 1544–1550.
- deQuilettes, D.W., Vorpahl, S.M., Stranks, S.D., Nagaoka, H., Eperon, G.E., Ziffer, M.E., Snaith, H.J., Ginger, D.S., 2015. Impact of microstructure on local carrier lifetime in perovskite solar cells. *Science* 348, 683–686.
- Domanski, K., Alharbi, E.A., Hagfeldt, A., Grätzel, M., Tress, W., 2018. Systematic investigation of the impact of operation conditions on the degradation behaviour of perovskite solar cells. *Nat. Energy* 3, 61–67. <https://www.nrel.gov/pv/cell-efficiency.html>, <https://www.nrel.gov/pv/cell-efficiency.html>.
- Hwang, K., Jung, Y.S., Heo, Y.J., Scholes, F.H., Watkins, S.E., Subbiah, J., Jones, D.J., Kim, D.Y., Vak, D., 2015. Toward large scale roll-to-roll production of fully printed perovskite solar cells. *Adv. Mater.* 27, 1241–1247.
- Im, J.-H., Lee, C.-R., Lee, J.-W., Park, S.-W., Park, N.-G., 2011. 6.5% efficient perovskite quantum-dot-sensitized solar cell. *Nanoscale* 3, 4088–4093.
- Jeon, N.J., Na, H., Jung, E.H., Yang, T.Y., Lee, Y.G., Kim, G., Shin, H.W., Seok, S.I., Lee, J., Seo, J., 2018. A fluorene-terminated hole-transporting material for highly efficient and stable perovskite solar cells. *Nat. Energy* 3, 682–689.
- Kim, D.H., Han, G.S., Seong, W.M., Lee, J.W., Kim, B.J., Park, N.G., Hong, K.S., Lee, S., Jung, H.S., 2015. Niobium doping effects on TiO₂ mesoscopic electron transport layer-based perovskite solar cells. *ChemSuschem* 8, 2392–2398.
- Kojima, A., Teshima, K., Shirai, Y., Miyasaka, T., 2009. Organometal halide perovskites as visible-light sensitizers for photovoltaic cells. *J. Am. Chem. Soc.* 131, 6050–6051.
- Kumar, Y., Jaramillo-Quintero, O.A., Jerónimo Rendon, J.J., Perez, T.D., Rincón, M.E., Mathew, X., 2019. Short duration high temperature thermal processing to reduce interfacial trapping states in perovskite solar cells obtained by a green route. *Sol. Energy* 189, 285–290.
- Lee, D.-S., Chen, Y.-W., 2014. Nano Ag/TiO₂ catalyst prepared by chemical deposition and its photocatalytic activity. *J. Taiwan Inst. Chem. Eng.* 45, 705–712.
- Li, Z., Klein, T.R., Kim, D.H., Yang, M.J., Berry, J.J., van Hest, M., Zhu, K., 2018. Scalable fabrication of perovskite solar cells. *Nat. Rev. Mater.* 3, 18017.
- Liang, C., Li, P.W., Zhang, Y.Q., Gu, H., Cai, Q.B., Liu, X.T., Wang, J.F., Wen, H., Shao, G.S., 2017. Mild solution-processed metal-doped TiO₂ compact layers for hysteresis-less and performance-enhanced perovskite solar cells. *J. Power Sources* 372, 235–244.
- Liu, A., Liu, K., Zhou, H., Li, H., Qiu, X., Yang, Y., Liu, M., 2018. Solution evaporation processed high quality perovskite films. *Sci. Bull.* 63, 1591–1596.
- Liu, X.T., Wu, Z.H., Zhang, Y.Q., Tsamis, C., 2019a. Low temperature Zn-doped TiO₂ as electron transport layer for 19% efficient planar perovskite solar cells. *Appl. Surf. Sci.* 471, 28–35.
- Liu, Z.F., Kruckemeier, L., Krogmeier, B., Klingebiel, B., Marquez, J.A., Levenko, S., Oz, S., Mathur, S., Rau, U., Unold, T., Kirchartz, T., 2019b. Open-Circuit Voltages Exceeding 1.26 V in Planar Methylammonium Lead Iodide Perovskite Solar Cells. *ACS Energy Lett.* 4, 110–117.
- Luo, D.Y., Yang, W.Q., Wang, Z.P., Sadhanala, A., Hu, Q., Su, R., Shivanna, R., Trindade, G.F., Watts, J.F., Xu, Z.J., Liu, T.H., Chen, K., Ye, F.J., Wu, P., Zhao, L.C., Wu, J., Tu, Y.G., Zhang, Y.F., Yang, X.Y., Zhang, W., Friend, R.H., Gong, Q.H., Snaith, H.J., Zhu, R., 2018. Enhanced photovoltage for inverted planar heterojunction perovskite solar cells. *Science* 360, 1442–1446.
- Nan, G.J., Zhang, X., Abdi-Jalebi, M., Andaji-Garmaroudi, Z., Stranks, S.D., Lu, G., Beljonne, D., 2018. How methylammonium cations and chlorine dopants heal defects in lead iodide perovskites. *Adv. Energy Mater.* 8, 1702754.
- Ponseca, C.S., Savenije, T.J., Abdellah, M., Zheng, K.B., Yartsev, A., Pascher, T., Harlang, T., Chabera, P., Pullerits, T., Stepanov, A., Wolf, J.P., Sundstrom, V., 2014. Organometal halide perovskite solar cell materials rationalized: ultrafast charge generation, high and microsecond-long balanced mobilities, and slow recombination. *J. Am. Chem. Soc.* 136, 5189–5192.
- Qi, X., Liu, G., Wang, D., Zhu, N., Zhang, Y., Zhang, Z., Wu, C., Li, X., Luo, W., Li, Y., Hu, H., Chen, Z., Xiao, L., Wang, S., Qu, B., 2019. Stable power output (PCE > 19%) of planar perovskite solar cells with PbCl₂ modification at the interface of SnO₂/CH₃NH₃PbI₃. *Org. Electron.* 74, 52–58.
- Rong, Y.G., Hu, Y., Mei, A.Y., Tan, H.R., Saidaminov, M.I., Seok, S.I., McGehee, M.D., Sargent, E.H., Han, H.W., 2018. Challenges for commercializing perovskite solar cells. *Science* 361, eaat8235.
- Schmidt, T.M., Larsen-Olsen, T.T., Carle, J.E., Angmo, D., Krebs, F.C., 2015. Upscaling of perovskite solar cells: fully ambient roll processing of flexible perovskite solar cells with printed back electrodes. *Adv. Energy Mater.* 5, 1500569.
- Son, D.Y., Kim, S.G., Seo, J.Y., Lee, S.H., Shin, H., Lee, D., Park, N.G., 2018. Universal approach toward hysteresis-free perovskite solar cell via defect engineering. *J. Am. Chem. Soc.* 140, 1358–1364.
- Stranks, S.D., Eperon, G.E., Grancini, G., Menelaou, C., Alcocer, M.J.P., Leijtens, T., Herz, L.M., Petrozza, A., Snaith, H.J., 2013. Electron-hole diffusion lengths exceeding 1 micrometer in an organometal trihalide perovskite absorber. *Science* 342, 341–344.
- Su, C.-H., Hu, C.-C., Sun, Y.-C.C., Hsiao, Y.-C., 2016. Highly active and thermo-stable anatase TiO₂ photocatalysts synthesized by a microwave-assisted hydrothermal method. *J. Taiwan Inst. Chem. Eng.* 59, 229–236.
- Tress, W., Yavari, M., Domanski, K., Yadav, P., Niesen, B., Baena, J.P.C., Hagfeldt, A., Grätzel, M., 2018. Interpretation and evolution of open-circuit voltage, recombination, ideality factor and subgap defect states during reversible light-soaking and irreversible degradation of perovskite solar cells. *Energy Environ. Sci.* 11, 151–165.
- Unger, E.L., Bowring, A.R., Tassone, C.J., Pool, V.L., Gold-Parker, A., Cheacharoen, R., Stone, K.H., Hoke, E.T., Toney, M.F., McGehee, M.D., 2014. Chloride in lead chloride-derived organo-metal halides for perovskite-absorber solar cells. *Chem. Mater.* 26, 7158–7165.
- Wang, J., Qin, M.C., Tao, H., Ke, W.J., Chen, Z., Wan, J.W., Qin, P.L., Xiong, L.B., Lei, H.W., Yu, H.Q., Fang, G.J., 2015a. Performance enhancement of perovskite solar cells with Mg-doped TiO₂ compact film as the hole-blocking layer. *Appl. Phys. Lett.* 106, 121104.
- Wang, K., Liu, C., Du, P., Chen, L., Zhu, J., Karim, A., Gong, X., 2015b. Efficiencies of perovskite hybrid solar cells influenced by film thickness and morphology of CH₃NH₃PbI_{3-x}Cl_x layer. *Org. Electron.* 21, 19–26.
- Wang, Q., Qiu, L., Tan, X., Liu, Z., Gao, S., Wang, R., 2019. Amorphous TiO₂ granular nanodisks on porous Ti foam for highly effective solar cells and photocatalysts. *J. Taiwan Inst. Chem. Eng.* 102, 85–91.
- Wu, M.-C., Chan, S.-H., Jao, M.-H., Su, W.-F., 2016a. Enhanced short-circuit current density of perovskite solar cells using Zn-doped TiO₂ as electron transport layer. *Sol. Energy Mater. Sol. Cells* 157, 447–453.
- Wu, M.-C., Chang, I.C., Hsiao, K.-C., Huang, W.-K., 2016b. Highly visible-light absorbing black TiO₂ nanocrystals synthesized by sol-gel method and subsequent heat treatment in low partial pressure H₂. *J. Taiwan Inst. Chem. Eng.* 63, 430–435.
- Wu, M.-C., Chang, Y.-H., Lin, T.-H., 2017. Bismuth doping effect on crystal structure and photodegradation activity of Bi-TiO₂ nanoparticles. *Jpn. J. Appl. Phys.* 56, 04CJ01.
- Wu, M.-C., Hsiao, K.-C., Chang, Y.-H., Chan, S.-H., 2018a. Photocatalytic hydrogen evolution of palladium nanoparticles decorated black TiO₂ calcined in argon atmosphere. *Appl. Surf. Sci.* 430, 407–414.
- Wu, M.-C., Liao, Y.-H., Chan, S.-H., Lu, C.-F., Su, W.-F., 2018b. Enhancing organolead halide perovskite solar cells performance through interfacial engineering using Ag-doped TiO₂ hole blocking layer. *Sol. RRL* 2, 1800072.
- Wu, M.-C., Chan, S.-H., Lee, K.-M., Chen, S.-H., Jao, M.-H., Chen, Y.-F., Su, W.-F., 2018c. Enhancing the efficiency of perovskite solar cells using mesoscopic zinc-doped TiO₂ as the electron extraction layer through band alignment. *J. Mater. Chem. A* 6, 16920–16931.
- Wu, M.-C., Lee, P.-H., Lee, D.-L., 2015. Enhanced photocatalytic activity of palladium decorated TiO₂ nanofibers containing anatase-rutile mixed phase. *Int. J. Hydrog. Energy* 40, 4558–4566.
- Wu, M.-C., Wu, P.-Y., Lin, T.-H., Lin, T.-F., 2018d. Photocatalytic performance of Cu-doped TiO₂ nanofibers treated by the hydrothermal synthesis and air-thermal treatment. *Appl. Surf. Sci.* 430, 390–398.
- Xiao, Y.Q., Cheng, N., Kondamareddy, K.K., Wang, C.L., Liu, P., Guo, S.S., Zhao, X.Z., 2017. W-doped TiO₂ mesoporous electron transport layer for efficient hole transport material free perovskite solar cells employing carbon counter electrodes. *J. Power Sources* 342, 489–494.
- Xing, G.C., Mathews, N., Sun, S.Y., Lim, S.S., Lam, Y.M., Grätzel, M., Mhaisalkar, S., Sun, T.C., 2013. Long-range balanced electron- and hole-transport lengths in organic-inorganic CH₃NH₃PbI₃. *Science* 342, 344–347.
- Xu, J., Voznyy, O., Comin, R., Gong, X., Walters, G., Liu, M., Kanjanaboos, P., Lan, X., Sargent, E.H., 2016. Crosslinked remote-doped hole-extracting contacts enhance stability under accelerated lifetime testing in perovskite solar cells. *Adv. Mater.* 28, 2807–2815.

- Yan, K.Y., Long, M.Z., Zhang, T.K., Wei, Z.H., Chen, H.N., Yang, S.H., Xu, J.B., 2015. Hybrid halide perovskite solar cell precursors: colloidal chemistry and coordination engineering behind device processing for high efficiency. *J. Am. Chem. Soc.* 137, 4460–4468.
- Yu, H., Wang, F., Xie, F.Y., Li, W.W., Chen, J., Zhao, N., 2014. The role of chlorine in the formation process of “CH₃NH₃PbI_{3-x}Cl_x” perovskite. *Adv. Funct. Mater.* 24, 7102–7108.
- Zeng, Q.S., Zhang, X.Y., Feng, X.L., Lu, S.Y., Chen, Z.L., Yong, X., Redfern, S.A.T., Wei, H.T., Wang, H.Y., Shen, H.Z., Zhang, W., Zheng, W.T., Zhang, H., Tse, J.S., Yang, B., 2018. Polymer-passivated inorganic cesium lead mixed-halide perovskites for stable and efficient solar cells with high open-circuit voltage over 1.3V. *Adv. Mater.* 30, 1705393.
- Zhang, H.Y., Shi, J.J., Xu, X., Zhu, L.F., Luo, Y.H., Li, D.M., Meng, Q.B., 2016. Mg-doped TiO₂ boosts the efficiency of planar perovskite solar cells to exceed 19%. *J. Mater. Chem. A* 4, 15383–15389.
- Zhang, X., Bao, Z.Q., Tao, X.Y., Sun, H.X., Chen, W., Zhou, X.F., 2014. Sn-doped TiO₂ nanorod arrays and application in perovskite solar cells. *RSC Adv.* 4, 64001–64005.
- Zhou, H., Chen, Q., Li, G., Luo, S., Song, T.-B., Duan, H.-S., Hong, Z., You, J., Liu, Y., Yang, Y., 2014. Interface engineering of highly efficient perovskite solar cells. *Science* 345, 542–546.
- Zhu, L., Shi, J., Li, D., Meng, Q., 2015. Effect of mesoporous TiO₂ layer thickness on the cell performance of perovskite solar cells. *Acta Chim. Sinica* 73, 261–266.
- Zhu, Y., Deng, K., Sun, H., Gu, B., Lu, H., Cao, F., Xiong, J., Li, L., 2018. TiO₂ phase junction electron transport layer boosts efficiency of planar perovskite solar cells. *Adv. Sci.* 5, 1700614.